

Significant Change of Metal Cations in Geometric Sites by Magnetic-Field Annealing FeCo_2O_4 for Enhanced Oxygen Catalytic Activity

Zhengmei Zhang, Junfu Li, Jinmei Qian, Zhiwei Li, Lei Jia, Daqiang Gao,*
and Desheng Xue*

The application of magnetic fields in the oxygen reduction/evolution reaction (ORR/OER) testing for electrocatalysts has attracted increasing interest, but it is difficult to characterize on-site surface reconstruction. Here, a strategy is developed for annealing-treated FeCo_2O_4 nanofibers at a magnetic field of 2500 Oe, named $\text{FeCo}_2\text{O}_4\text{-M}$, showing a right-shifted half-wave potential of 20 mV for the ORR and a left-shifted overpotential of 60 mV at 10 mV cm^{-2} for the OER as compared with its counterpart. Magnetic characterizations indicate that $\text{FeCo}_2\text{O}_4\text{-M}$ shows the spin-state transition of cations from a low-spin state to an intermediate-spin state compared with FeCo_2O_4 . Mössbauer spectra show that the Fe^{3+} ion in the octahedral site (0.76) of $\text{FeCo}_2\text{O}_4\text{-M}$ is more than that of FeCo_2O_4 (0.71), indicating the effective stimulus of metal cations in geometric sites by magnetic-field annealing. Furthermore, theoretical calculations demonstrate that the d-band centers (ϵ_d) of Co 3d and Fe 3d in the tetrahedral and octahedral sites of the $\text{FeCo}_2\text{O}_4\text{-M}$ nanofibers shift close to the Fermi level, revealing the enhanced mechanism of the ORR/OER activity.

OER).^[6,7] Ideally, remarkable ORR/OER bifunctional electrocatalysts should have excellent catalytic activity, stability, and economic feasibility.^[8–11] In recent years, increasing attention has been paid to spinel oxides (AB_2O_4), which are excellent oxygen electrocatalysts with distinct d-band electronic configurations.^[12–20] In the spinel lattice, A^{2+} and B^{3+} ions occupy the tetrahedron and octahedron, and they are surrounded by four and six oxygen anions, respectively. Spinel, represented by $(\text{A}_{1-x}\text{B}_x)_{\text{Tet}}(\text{A}_x\text{B}_{2-x})_{\text{Oct}}\text{O}_4$, is an open structure owing to one-eighth of the tetrahedral and half of the octahedral interstices filled with metal ions, while the remaining unoccupied interstices are conducive to the migration of metal ions.^[14,21] The inversion degree (x) determines the distribution of the two metal ions, which can further affect the chemical and physical properties of the spinel.^[22–24]


1. Introduction

Zn–air batteries (ZABs) have been widely used in energy storage systems owing to their high energy density, inexpensive, environmental friendliness, and intrinsic safety.^[1–5] The wide-ranging applications of ZABs are limited by their low energy conversion efficiencies and high anodic overpotentials. These shortcomings are primarily caused by the sluggish kinetics of the oxygen reduction/evolution reaction (ORR/

Adjusting the tetrahedral and octahedral occupancy of metal ions is an outstanding strategy for improving the electrochemical properties of AB_2O_4 .^[22,25–27] A general rule summarized in the literature is that the active cations in the octahedral sites dominate the electrocatalytic activity of spinel oxides. The e_g orbital occupancy or 3d-band center of active cations also plays a key role in the ORR/OER progress of spinel oxides. Recently, Gracia proposed that the e_g electron in the active site of perovskite has a prominent contribution to its magnetic moment, which is also a descriptor for OER catalysis.^[28] Generally, octahedral cations of spinel and perovskite cobalt-based materials exist in the form of Co^{3+} . Co^{3+} in CoO_6 has a low spin ($t_{2g}^6e_g^0$) as per the crystal field theory, where the 3d-electrons are completely paired, resulting in a net magnetic moment of zero.^[26] However, the effective magnetic moment increases significantly with the intermediate-spin state ($t_{2g}^5e_g^1$) of Co^{3+} in the octahedral site, which can be magnetically polarized.^[10] Recently, the application of an external magnetic field during catalytic process for magnetic catalyst has received much attention, as it can change the spin polarization by accelerating the electron transitions from low-spin states to high-spin states,^[29] enhancing the spin selection,^[30] and thereby having a positive effect on the ORR/OER progress of the catalysts.^[29–31] Coincidentally, magnetic moments related to the extrinsic spin polarization of magnetic

Z. Zhang, J. Li, J. Qian, Z. Li, L. Jia, D. Gao, D. Xue
Key Laboratory for Magnetism and Magnetic Materials of Ministry of Education
Lanzhou University
Lanzhou 730000, P. R. China
E-mail: gaodq@lzu.edu.cn; xueds@lzu.edu.cn

Z. Zhang
Key Laboratory of Atomic and Molecular Physics & Function Material of Gansu Province
Northwest Normal University
Lanzhou 730070, P. R. China

 The ORCID identification number(s) for the author(s) of this article can be found under <https://doi.org/10.1002/smll.202104248>.

DOI: 10.1002/smll.202104248

oxides can also be induced by annealing them in an extra magnetic field,^[32–34] however, this strategy is rarely applied for the ORR/OER progress in electrocatalysts. Therefore, magnetic field annealing-treated magnetic electrocatalysts to enhanced ORR/OER activity by adjusting geometric sites with spin-state transition is expected.

Here, we used annealing-treated spinel FeCo_2O_4 nanofibers without a magnetic field (denoted FeCo_2O_4) and FeCo_2O_4 nanofibers annealed in an extra magnetic field (denoted $\text{FeCo}_2\text{O}_4\text{-M}$) as model samples, where the geometric sites of the Fe and Co cations clearly changed, thus leading to enhanced ORR/OER electrocatalytic activity and stability. The surface properties of FeCo_2O_4 and $\text{FeCo}_2\text{O}_4\text{-M}$ were characterized by X-ray absorption fine structure spectroscopy (XAFS) and X-ray photoelectron spectroscopy (XPS), where the enhancement of the oxidation state for cobalt ions and the change in the coordination environment highlight the advantage of magnetic-field annealing. Meanwhile, we focus on first-principles calculations to compare the d-band centers (ϵ_d) of Co 3d and Fe 3d in tetrahedral and octahedral sites for FeCo_2O_4 and $\text{FeCo}_2\text{O}_4\text{-M}$. The smaller ϵ_d of $\text{FeCo}_2\text{O}_4\text{-M}$ facilitates the adsorption of electrocatalysis intermediates, thus promoting the ORR/OER activity. Finally, the assembled ZAB based on $\text{FeCo}_2\text{O}_4\text{-M}$ displayed better cycling stability and superior properties compared to the FeCo_2O_4 -based and commercial Pt/C–Ir/C-based ZABs.

2. Results and Discussion

Figure 1a shows a schematic illustration of the preparation of $\text{FeCo}_2\text{O}_4\text{-M}$. The initial FeCo_2O_4 nanofibers were prepared by electrospinning, followed by calcination in air, and then, the obtained FeCo_2O_4 -initial nanofibers were treated by applying

a magnetic field of 2500 Oe at 550 °C in vacuum (denoted as $\text{FeCo}_2\text{O}_4\text{-M}$). The FeCo_2O_4 nanofibers were annealing at 550 °C for 1 h (denoted as FeCo_2O_4) for comparison, as shown in the Experimental Section of the Supporting Information. We first investigated the magnetic properties of both samples, where the magnetic hysteresis (M-H) loops of FeCo_2O_4 , and $\text{FeCo}_2\text{O}_4\text{-M}$ were characterized by using a vibrating sample magnetometer (VSM) at room temperature, as shown in Figure 1b. The saturated magnetization (M_s) of 25.1 emu g^{-1} for $\text{FeCo}_2\text{O}_4\text{-M}$ is larger than that of FeCo_2O_4 (20.9 emu g^{-1}), indicating a reinforcement of magnetic moments aligning the direction of applying strong field with the achievement of a higher spin-state. To further insight into the electron spin configuration of the samples, zero-field-cooled (ZFC) and field-cooled (FC) measurements were performed under a 20 000 Oe magnetic field, as shown in Figure 1c, and the magnetization trend was in a good agreement with the VSM results. Figure 1d shows that the reciprocal susceptibilities (χ^{-1}) are derived from the FC curves of FeCo_2O_4 and $\text{FeCo}_2\text{O}_4\text{-M}$, respectively. The calculated effective magnetic moment (μ_{eff}) of $\text{FeCo}_2\text{O}_4\text{-M}$ (2.82 μ_B) was larger than that of FeCo_2O_4 (2.70 μ_B), as per Curie Weiss's law $\chi = C/(\theta + T)$, where C is the Curie constant, and θ is the Curie–Weiss constant.^[35–37] The increase in μ_{eff} related to more unpaired electrons illustrates a transition of the spin-state of the metal ions, e.g., from a low-spin state ($t_{2g}^5e_g^0$) to an intermediate-spin state ($t_{2g}^4e_g^1$) for Fe^{3+} , and from $t_{2g}^6e_g^0$ to $t_{2g}^5e_g^1$ for Co^{3+} . Existing experimental studies reveal that the spin polarization of electrons in the outermost orbit can be promoted by applying an extra magnetic field with more unpaired electrons in the 3d-orbit.^[38–40] The kinetics of the oxygen catalytic performance can be affected by the change in magnetism related to the spin polarization of metallic oxides;^[41,42] thus, optimizing the spin-state after magnetic field annealing treatment can favor the oxygen catalytic effect.

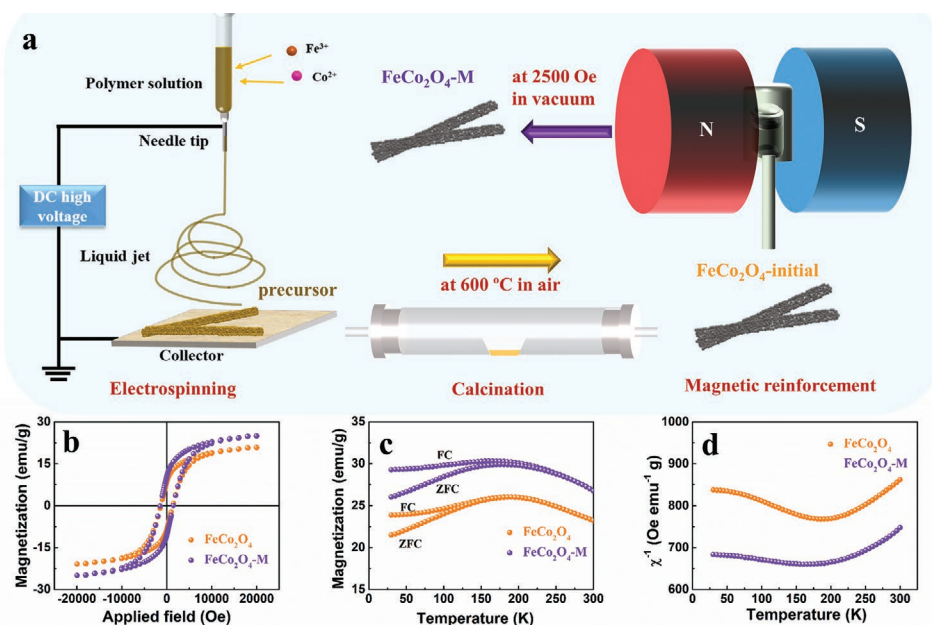


Figure 1. a) Schematic illustration of FeCo_2O_4 and $\text{FeCo}_2\text{O}_4\text{-M}$. b) Magnetic hysteresis loops, c) ZFC/FC curves, and d) temperature-dependent reciprocal magnetic susceptibilities of FeCo_2O_4 and $\text{FeCo}_2\text{O}_4\text{-M}$.

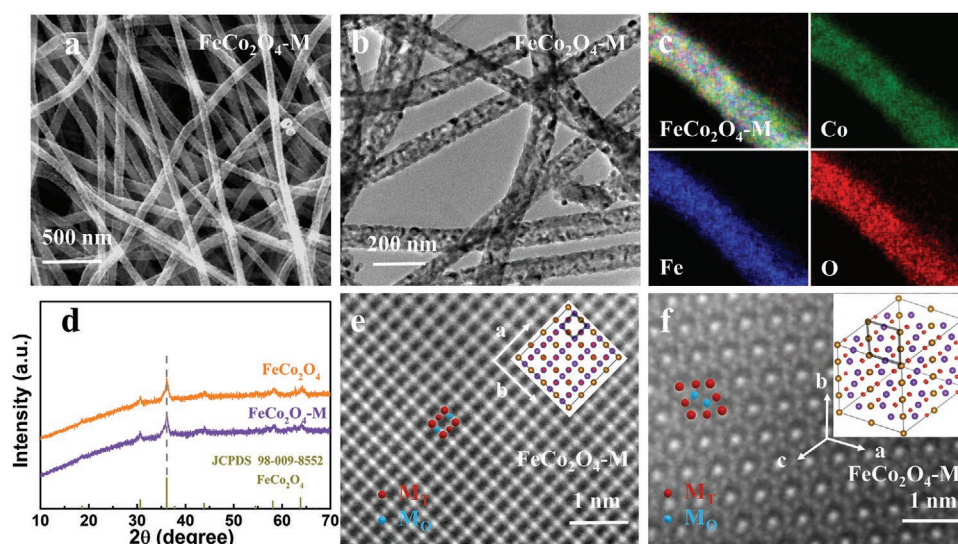


Figure 2. $\text{FeCo}_2\text{O}_4\text{-M}$: a) SEM image, b) TEM image, and c) EDX mappings. d) X-ray diffraction (XRD) patterns. e, f) STEM atomic view; insets are the crystal structure of $\text{FeCo}_2\text{O}_4\text{-M}$, where M_T represents Fe, Co occupy tetrahedrons, and M_O represents Fe, Co occupy octahedrons.

Scanning electron microscopy (SEM) (Figure 2a; Figure S1, Supporting Information) and transmission electron microscopy (TEM; Figure 2b) analyses were performed to investigate the morphologies of FeCo_2O_4 and $\text{FeCo}_2\text{O}_4\text{-M}$. FeCo_2O_4 shows the morphology of nanofibers with a diameter of ≈ 110 nm formed by the aggregation of a large number of nanoparticles. After magnetic-field annealing, the morphology of $\text{FeCo}_2\text{O}_4\text{-M}$ remained unchanged, with a rough and porous surface. The Fe, Co, and O elements are distributed homogeneously in the nanofibers, as revealed from the elemental mapping of $\text{FeCo}_2\text{O}_4\text{-M}$ by energy-dispersive X-ray spectroscopy (EDX; see Figure 2c). The diffraction peaks of FeCo_2O_4 and $\text{FeCo}_2\text{O}_4\text{-M}$ are correspond to those of spinel FeCo_2O_4 (JCPDS card No: 98-009-8552) (Figure 2d). Further, probe aberration-corrected scanning transmission electron microscopy (STEM) images are

shown in Figure 2e,f, and Figure S2 in the Supporting Information shows the atomic structure of $\text{FeCo}_2\text{O}_4\text{-M}$, revealing the random distribution of the FeCo_2O_4 phase views along the [110] and [111] crystallographic orientations, respectively.

To verify the effectiveness of the change in magnetism related to spin polarization on the electrocatalytic performance, ORR/OER tests were carried out for FeCo_2O_4 and $\text{FeCo}_2\text{O}_4\text{-M}$ using a three-electrode system. Rotating disk electrodes (RDEs) and rotating ring-disk electrodes (RRDEs) were explored to evaluate the ORR performance. The CV curves in the O_2 -saturated KOH solution indicated that FeCo_2O_4 and $\text{FeCo}_2\text{O}_4\text{-M}$ have electrochemical oxygen reduction capacity with a significant current response (Figure S3, Supporting Information). As shown in Figure 3a, the RDE linear scan voltammetry (LSV) curves at 1600 rpm revealed a higher onset potential (0.91 V), half-wave

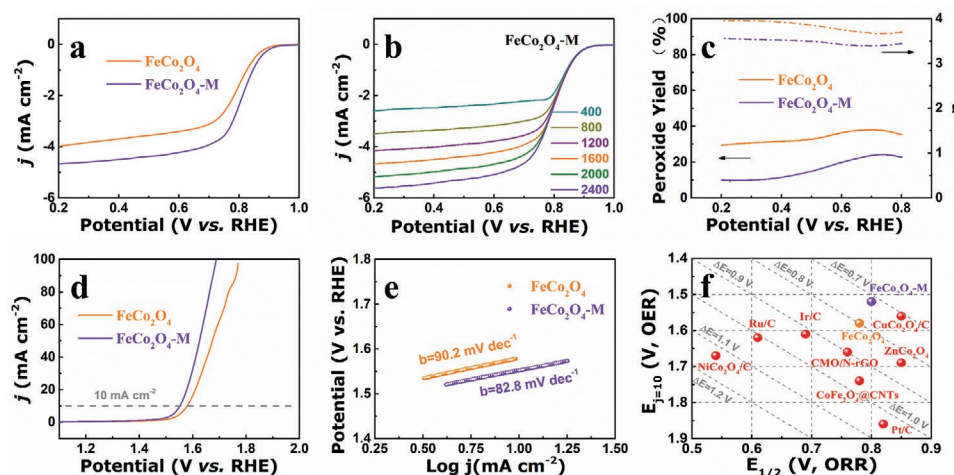


Figure 3. a) ORR LSV curves of FeCo_2O_4 and $\text{FeCo}_2\text{O}_4\text{-M}$ at 1600 rpm. b) ORR LSV curves of $\text{FeCo}_2\text{O}_4\text{-M}$ at different rotational speeds. c) Peroxide percentage and calculated n of FeCo_2O_4 and $\text{FeCo}_2\text{O}_4\text{-M}$. d) OER LSV curves, and e) Tafel slopes of FeCo_2O_4 and $\text{FeCo}_2\text{O}_4\text{-M}$. f) ORR and OER performances in this work compared with catalysts in references.

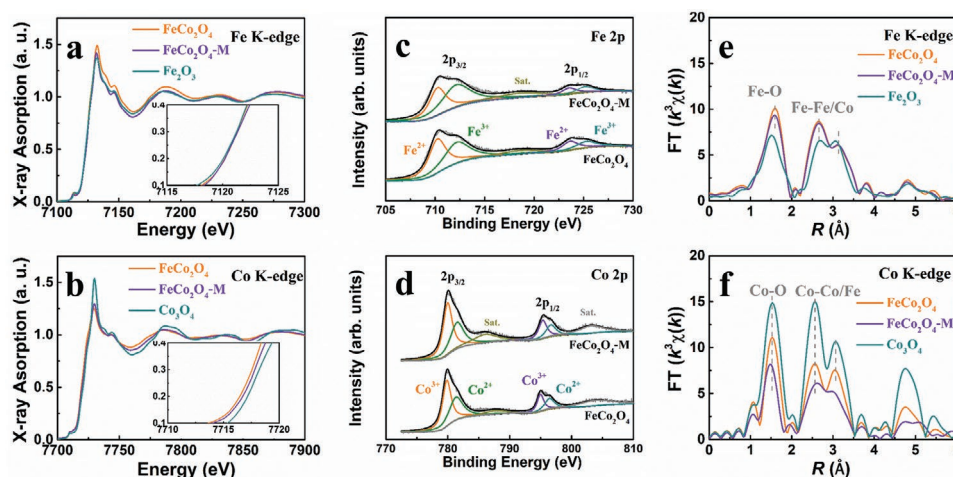


Figure 4. FeCo₂O₄ and FeCo₂O₄-M: a) Fe K-edge and b) Co K-edge XANES spectra; c) Fe 2p and d) Co 2p XPS spectra; Fourier transformed extended XAFS spectra at e) Fe K-edge and f) Co K-edge.

potential ($E_{1/2}$, 0.80 V) and limiting current density (j_L , 4.68 mA cm⁻²) of FeCo₂O₄-M than those (0.90 V, 0.78 V, 3.98 mA cm⁻²) of FeCo₂O₄. Accordingly, the mass diffusion-corrected Tafel slope of FeCo₂O₄-M (74.6 mV dec⁻¹) is superior that for FeCo₂O₄ (78.4 mV dec⁻¹), as shown in Figure S4 in the Supporting Information. Besides, Figure S5 in the Supporting Information and Figure 3b present the ORR LSV curves of FeCo₂O₄ and FeCo₂O₄-M at different rotational speeds. It can be seen that the current density increases with rotational speeds, indicating ORR is a first-order reaction. The Koutechy–Levich (K–L) plots obtained from LSV curves reveal good linear relationships, indicating that the ORR at different potentials to dissolved oxygen follows first-order dynamics, and the electron transfer numbers (n) are similar (Figure S6, Supporting Information). The n values obtained from the K–L equations of FeCo₂O₄ and FeCo₂O₄-M are \approx 3.43 and 3.80, respectively, indicating adequate oxygen reduction of the nanofibers through a four-electron pathway. This pathway and mechanism were further investigated by RRDE measurements (Figure S7, Supporting Information). As shown in Figure 3c, the mean n of FeCo₂O₄-M is \approx 3.88, which is larger than that of FeCo₂O₄ (3.49) from 0.2 to 0.8 V versus RHE. Meanwhile, the evolution of hydrogen peroxide in FeCo₂O₄-M (9.8%) is greater extent than 29.9% of FeCo₂O₄. The abovementioned results demonstrate that the catalyst after magnetic-field annealing possesses enhanced ORR activity due to the faster ORR kinetics and is more conducive to the ORR process. The FeCo₂O₄ and FeCo₂O₄-M exhibit outstanding ORR stability, which was evaluated by the almost overlapped $E_{1/2}$ and j_L after 5000 cycles and maintained above 95% in the current density retention rate after 35 000 s (Figure S8, Supporting Information).

Further, to demonstrate the bifunctional performance of FeCo₂O₄-M, its OER activity was evaluated using LSV curves. As shown in Figure 3d,e, FeCo₂O₄-M displays superior OER activity with a smaller onset potential (1.48 V), overpotential at 10 mA cm⁻² ($E_j = 10$, 290 mV) and Tafel slope (82.8 mV dec⁻¹) compared with FeCo₂O₄ (1.51 V, 350 mV, 90.2 mV dec⁻¹). The charge transfer resistance (R_{ct}) of FeCo₂O₄-M (20.9 Ω) is smaller than that of FeCo₂O₄ (60.0 Ω), as confirmed by

electrochemical impedance spectroscopy (EIS) measurements, indicating a higher transfer rate of electrons during the OER process (Figure S9, Supporting Information). In addition, to evaluate the effective active sites, the double-layer capacitances (C_{dl}) proportional to the electrochemically active surface area (ECSA) were obtained from the CV curves, as shown in Figures S10 and S11 in the Supporting Information. The C_{dl} value of FeCo₂O₄-M (22.1 mF cm⁻²) was larger than that of FeCo₂O₄ (15.4 mF cm⁻²). The durability of FeCo₂O₄ before and after magnetization is excellent, which can be proved by the almost completely overlapped LSV curves over 5000 cycles and negligible change in the current density after 80 000 s (Figure S12, Supporting Information). The lower values of OER and ORR ($\Delta E = E_j = 10 - E_{1/2}$) can provide a more intuitive view of the better reversible oxygen electrocatalytic activity of bifunctional catalysts. As shown in Figure 3f and Table S1 in the Supporting Information, the FeCo₂O₄-M exhibits the smallest ΔE of 0.72 V among those of FeCo₂O₄ (0.80 V) and the Co-based spinel structure multifunctional electrocatalysts reported in the literature, further indicating that FeCo₂O₄-M shows excellent ORR/OER performance. From the previous characterization, given there are no obvious differences in the morphology of both samples, we deduce that the improved electrocatalytic properties of FeCo₂O₄-M may be due to microstructural changes.

Next, to explore the changes in the microstructure of both samples, XAFS measurements were carried out. As shown in Figure 4a, there was no significant difference in the Fe K-edge X-ray absorption near-edge structure spectroscopy (XANES) profiles for FeCo₂O₄ and FeCo₂O₄-M, confirming the preservation of the phase after magnetic-field annealing. The average valence states of Fe for FeCo₂O₄ and FeCo₂O₄-M were close to that of Fe³⁺, as referenced for Fe₂O₃. In contrast, the Co K-edge of FeCo₂O₄-M shifted positively compared to that of FeCo₂O₄, indicating an increased oxidation state of Co in FeCo₂O₄-M (Figure 4b). Note that the Co K-edges of FeCo₂O₄ and FeCo₂O₄-M are both smaller than that of standard Co₃O₄ because Fe³⁺ replaced some of the octahedral Co³⁺ sites in Co₃O₄. The maintenance valences of FeCo₂O₄ and FeCo₂O₄-M were further confirmed by XPS measurements. The survey spectra with the

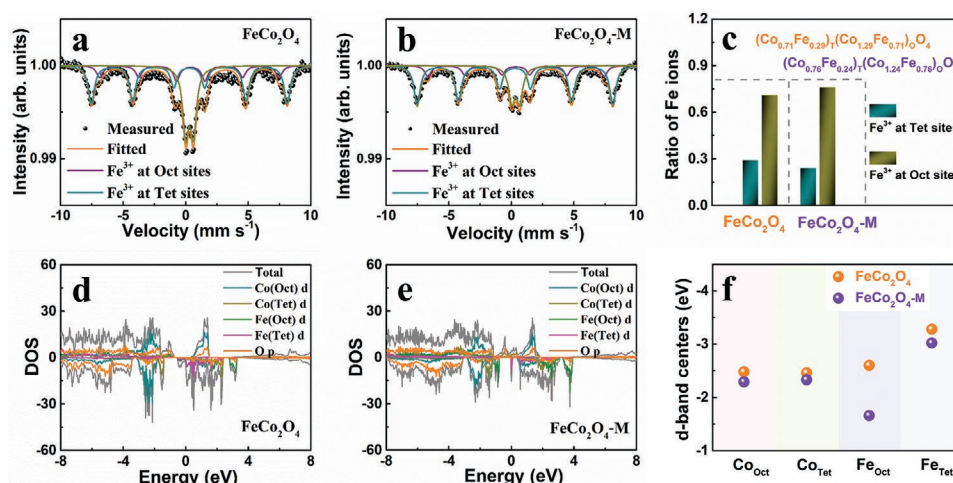


Figure 5. Mössbauer spectra of a) FeCo_2O_4 and b) $\text{FeCo}_2\text{O}_4\text{-M}$ at room temperature. c) Ratio of Fe ions and actual components for FeCo_2O_4 and $\text{FeCo}_2\text{O}_4\text{-M}$. DOS diagrams of d) FeCo_2O_4 and e) $\text{FeCo}_2\text{O}_4\text{-M}$. f) D-band center values of FeCo_2O_4 and $\text{FeCo}_2\text{O}_4\text{-M}$.

characteristic peaks of Fe 2p, Co 2p, and O 1s are shown in Figure S13a in the Supporting Information. Fe mainly existed in the trivalent form, as confirmed by analyzing the Fe 2p peaks (Figure 4c; Table S2, Supporting Information). The relative intensities of $\text{Fe}^{3+}/\text{Fe}^{2+}$ were very close between FeCo_2O_4 (2.95) and $\text{FeCo}_2\text{O}_4\text{-M}$ (2.97). Meanwhile, as shown in Figure 4d and Table S3 in the Supporting Information, the relative intensity of $\text{Co}^{3+}/\text{Co}^{2+}$ for $\text{FeCo}_2\text{O}_4\text{-M}$ (1.33) is superior to that of FeCo_2O_4 (1.19), suggesting a higher oxidation state of Co after magnetic-field annealing, confirming the results of XANES. In Figure S13b and Table S4 in the Supporting Information, the O 1s spectrum of O1, O2, and O3 represents the metal–oxygen bond, the surface oxygen (MOH/MOOH), and the surface-absorbed H_2O , respectively. The increased proportion of MOH/MOOH for $\text{FeCo}_2\text{O}_4\text{-M}$ (25.5%) compared with 23.4% for FeCo_2O_4 reveals its increased oxygen adsorption capacity and thus enhanced OER/ORR activity.^[43,44]

The Fourier transform (FT) extended XAFS (EXAFS) spectra of FeCo_2O_4 and $\text{FeCo}_2\text{O}_4\text{-M}$ are shown in Figure 4e,f. In the R space plots of Fe K-edge, the main peak located at 1.59 Å represents the Fe–O bond, meanwhile, peaks located at 2.60 and 3.11 Å represent the single scattering of Fe–Fe, or Fe–Co bonds due to the similar coordination of Co and Fe (Figure 4e). The intensity of the Fe–O peak and Fe–Fe/Co bond at 2.60 Å in $\text{FeCo}_2\text{O}_4\text{-M}$ decreases, revealing the decreased of oxygen ligands and the increase of disorder degree. Furthermore, in the Co plots (Figure 4f), the position of the Co–O bond shifts negatively to 1.91 Å ($\text{FeCo}_2\text{O}_4\text{-M}$) compared with that for FeCo_2O_4 (1.92 Å), implying an increase in the oxidation state of Co, corresponding to the results of XPS and XANES. The enhanced oxidation state of Co increases the possibility of dragging electrons from the O atom, thus optimizing the Co–O covalency.^[45] Meanwhile, the intensities of all peaks for the Co K-edge of $\text{FeCo}_2\text{O}_4\text{-M}$ are lower than those of the peaks for FeCo_2O_4 , revealing a decrease in the coordination number for Co.^[45,46] Thus, the difference in the XAFS spectra further suggests that the metal ion coordination environment is different between FeCo_2O_4 and $\text{FeCo}_2\text{O}_4\text{-M}$.

In order to study the possibility of coordination differences and structural changes of Fe in the nanocrystalline particles,

the Mössbauer spectra of FeCo_2O_4 and $\text{FeCo}_2\text{O}_4\text{-M}$ measured at room temperature are shown in Figure 5a,b, and the fitting hyperfine parameters are listed in Table S5 in the Supporting Information. The presence of the middle doublet with zero hyperfine fields represents the appearance of a paramagnetic phase due to a wide particle size distribution with smaller particles (<10 nm) of crystallite sizes. The average crystallite size of FeCo_2O_4 is ≈ 15 nm, as determined from the XRD results using the Scherrer formula,^[47] which probably corresponds to the ferrite phase.^[20] At the same time, the spectrum can be fitted with two sextets, attributed to the Fe ions occupying tetrahedrons and octahedrons. The values (about 0.3 mm s^{-1}) of the isomer shift indicate that the Fe ion is mainly in the trivalent form.^[48] Fe^{3+} ions occupying the tetrahedrons cause the sextet of FeCo_2O_4 with a smaller magnetic hyperfine field of 44.6 T, and Fe^{3+} ions at the octahedron are assigned to a sextet with a maximum magnetic hyperfine field of 48.6 T. The simultaneous presence of Fe^{3+} ions in tetrahedrons and octahedrons indicates that FeCo_2O_4 and $\text{FeCo}_2\text{O}_4\text{-M}$ are hybrid spinels $(\text{Co}_{0.71}\text{Fe}_{0.29})_{\text{T}}(\text{Co}_{1.29}\text{Fe}_{0.71})_{\text{O}}\text{O}_4$ and $(\text{Co}_{0.76}\text{Fe}_{0.24})_{\text{T}}(\text{Co}_{1.24}\text{Fe}_{0.76})_{\text{O}}\text{O}_4$, respectively (Figure 5c).

The overall d-band centers (ε_d) are regulated by replacing partial Co octahedrons with Fe octahedrons with a high d-band, thus optimizing the oxygen catalytic activity.^[49] To confirm this point, first-principles calculations of the band structures of the above cases were performed. The ε_d relative to the Fermi level (E_f) is a vital indicator of the intrinsic electrocatalytic performance of transition metal catalysts.^[49,50] The adsorption on the electrocatalyst surface becomes stronger as ε_d approaches E_f . The density-of-states (DOS) of the two samples are displayed in Figure 5d,e. In the theoretical model, different doping concentrations were allowed to be realized. We chose a suitable cell with the closest concentration of the actual sample, such as $(\text{Co}_{0.5}\text{Fe}_{0.5})_{\text{T}}(\text{Co}_{1.5}\text{Fe}_{0.5})_{\text{O}}\text{O}_4$ and $(\text{Co}_{0.75}\text{Fe}_{0.25})_{\text{T}}(\text{Co}_{1.25}\text{Fe}_{0.75})_{\text{O}}\text{O}_4$ represent FeCo_2O_4 , and $\text{FeCo}_2\text{O}_4\text{-M}$, respectively. As shown in Figure 5f and Table S6 in the Supporting Information, the ε_d of Co 3d in B (−2.29 eV) and A sites (−2.33 eV) for $\text{FeCo}_2\text{O}_4\text{-M}$ is close to the E_f of FeCo_2O_4 nanofibers (B sites: −2.48 eV; A sites: −2.46 eV), respectively. The ε_d of Fe 3d was also calculated,

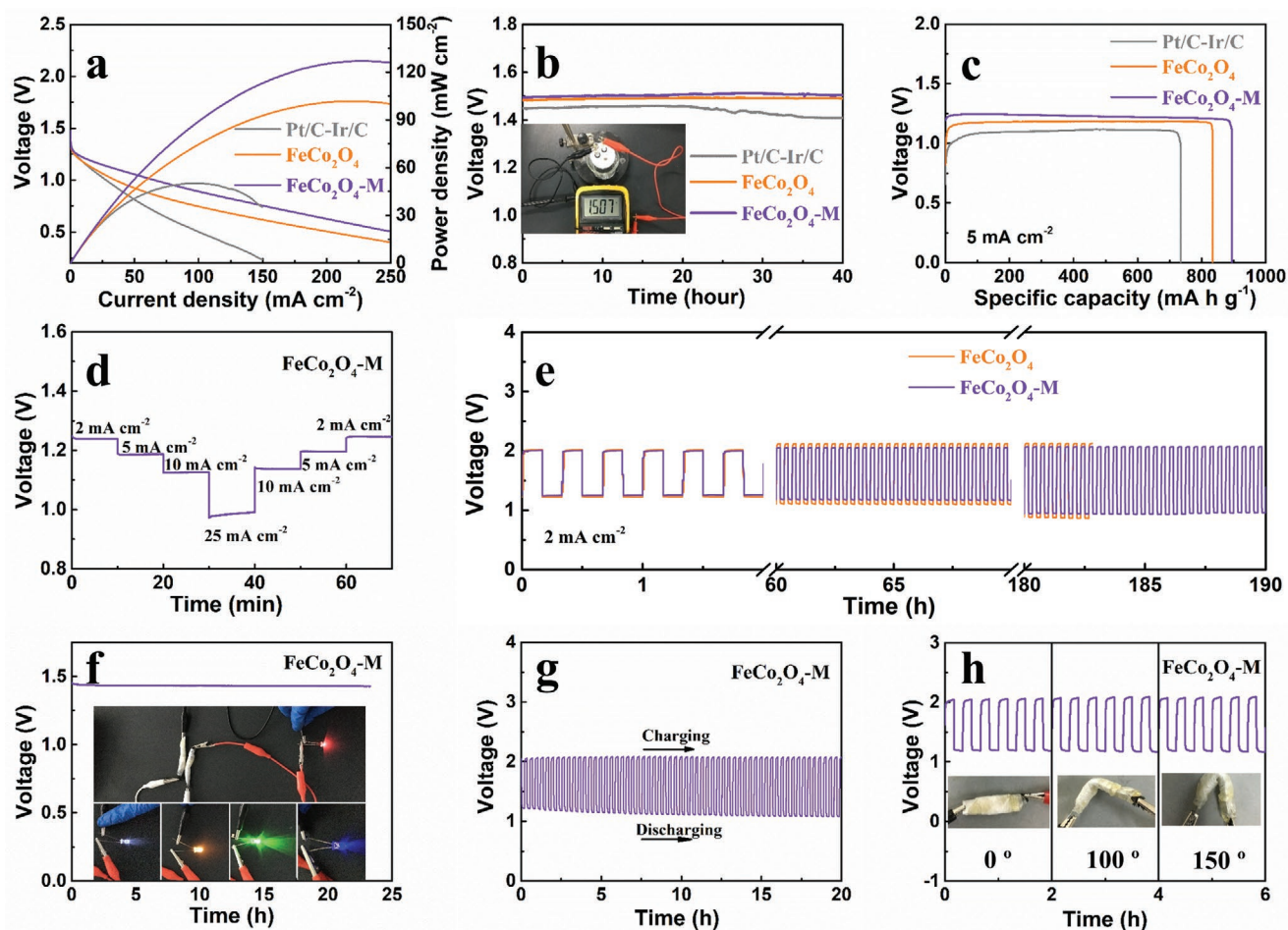


Figure 6. a) Discharge polarization and power density curves, b) open potential, and c) specific capacity of the Pt/C-Ir/C, FeCo₂O₄, and FeCo₂O₄-M-based ZABs. d) Discharge curves of FeCo₂O₄-M-based ZABs. e) Charge and discharge performance of FeCo₂O₄ and FeCo₂O₄-M-based ZABs. f) Open potential, g) charge and discharge performance, and h) cycling performance bending to 0°, 100°, and 150° of flexible battery based on FeCo₂O₄-M nanofibers cathode.

which showed the same changing trend. Thus, the above results clearly illustrate that the ϵ_d values of Co 3d and Fe 3d in the A and B sites shifted close to E_f with the increase in Fe³⁺ ions occupying the B sites upon applying a magnetic field, which can increase binding and optimize the efficiency of electron transfer between the adsorbed oxygen species and metal cations, and thus favorably tune the oxygen catalytic efficiency.

Finally, based on the favorable OER/ORR catalytic activity of FeCo₂O₄-M, ZABs with FeCo₂O₄ and FeCo₂O₄-M as the cathodes were assembled. The schematic of an aqueous ZAB is shown in Figure S14 in the Supporting Information. The FeCo₂O₄-M-based ZAB has the smallest discharging–charging voltage difference and the greatest power density (127.3 mW cm⁻²) compared to the FeCo₂O₄ (101.6 mW cm⁻²) and the commercial Pt/C-Ir/C (50.4 mW cm⁻²)-based ZABs, as shown in Figure 6a and Figure S15 in the Supporting Information, indicating the favorable charge–discharge performance of FeCo₂O₄-M ZAB. The FeCo₂O₄-M and FeCo₂O₄-based ZAB can work steadily for at least 40 h with an open potential of 1.51 and 1.49 V, respectively. The inferior open potential of 1.46 V for commercial Pt/C-Ir/C ZAB only work steadily for 20 h (Figure 6b). As

shown in Figure 6c, the FeCo₂O₄-M-based ZAB has an excellent specific capacity (SC) of 851.9 mA h g⁻¹ at 5 mA cm⁻², corresponding to an outstanding gravimetric specific energy of 996.2 W h kg⁻¹, which is about 91.7% of the theoretical value. The SC of the FeCo₂O₄-based ZAB also reaches a higher value (817.6 mA h g⁻¹) than that of commercial Pt/C-Ir/C-based ZAB (735.0 mA h g⁻¹). The SC of FeCo₂O₄-M and FeCo₂O₄-based ZABs retain 813.0 and 760.5 mA h g⁻¹ at 10 mA cm⁻², respectively, showing their superior rate capability (Figure S16, Supporting Information). In addition, the potential drop of the FeCo₂O₄-M-based ZAB is smaller than that of FeCo₂O₄ and the Pt/C-Ir/C-based ZABs at 2 to 25 mA cm⁻² in the galvanostatic discharging measurement. Meanwhile, the potential reversibly resumes once the current density decreases to a low value, demonstrating outstanding discharge rate performance (Figure 6d; Figure S17, Supporting Information). Zinc acetate (0.2 M) was added to the electrolyte to further evaluate the cycling stability of the ZABs. As shown in Figure 6e, the FeCo₂O₄-M-based ZAB with a smaller initial voltage gap (VG) of 0.75 V is more stable than the FeCo₂O₄-based ZAB (0.79 V) at

2 mA cm⁻². The energy efficiency of FeCo₂O₄-M-based ZAB is 51.7% with a small VG of 1.00 V after continuous 400 cycles. In comparison, FeCo₂O₄-based ZAB shows great degradation with a small energy efficiency of 48.8% with a voltage gap of 1.10 V (Figure S18, Supporting Information), and the zinc plate break-ages after 182.5 h of continuous cycling.

With the imperious demand for flexible energy-storage products, we have also constructed a flexible ZAB with FeCo₂O₄-M as the cathode; the schematic is shown in Figure S19 in the Supporting Information. The assembled FeCo₂O₄-M-based flexible ZAB displays a good open potential of 1.43 V, and a flexible ZAB pack with two batteries can supply red, white, yellow, green, and blue LEDs to light, as shown in Figure 6f. The flexible ZAB is stable with a small initial VG (0.84 V), corresponding charge (2.06 V), and discharge (1.22 V) at 2 mA cm⁻². After 20 h continuous cycling, the high energy efficiency is 52.7% with a small VG of 0.98 V (Figure 6g). As shown in Figure 6h, the performance of the flexible ZAB was estimated under different bending angles. The results demonstrate that ZAB revealed excellent cycling stability when the bending angles were 0°, 100°, and 150°. These results indicate that the magnetic field annealing-treated FeCo₂O₄ has superior electrocatalytic activity and stability, which can make the flexible ZAB, based on the nanofiber cathode, show outstanding performance and stability.

3. Conclusions

In summary, spinel FeCo₂O₄-M nanofibers with enhanced ORR/OER and excellent performance for ZABs have been reported. We demonstrate that magnetic field annealing treatment is an outstanding way to change the geometric sites of metal cations, and thus enhance the intrinsic activity of electrocatalysis. The magnetic field annealing-treated-FeCo₂O₄ nanofibers possess unique surface properties with a higher oxidation state and changed coordination environment, as proven by XAFS and XPS. Meanwhile, the experimental and theoretical results confirm that the main reason for the improvement in oxygen catalytic activity is the change in the occupancy of Co³⁺ and Fe³⁺ ions with smaller d-band centers in the tetrahedral and octahedral sites after magnetic-field annealing. This finding provides a new method for optimizing magnetic electrocatalysts and thus enhancing the ORR/OER performance for wider applications in energy storage and conversion systems.

Supporting Information

Supporting Information is available from the Wiley Online Library or from the author.

Acknowledgements

This work was supported by the Program for Changjiang Scholars and Innovative Research Team in University (Grant No. IRT-16R35), the Natural Science Foundation (NSF) of China (Grant No. 91963201), the 111 Project under Grant No. B20063, and the NSF of Gansu Province China (Grant Nos. 20JR5RA303 and 20JR10RA648).

Conflict of Interest

The authors declare no conflict of interest.

Data Availability Statement

Research data are not shared.

Keywords

d-band center, FeCo₂O₄ nanofibers, magnetic field application, Zn–air batteries

Received: July 19, 2021
Revised: November 9, 2021
Published online:

- [1] J. Yin, J. Jin, H. Liu, B. Huang, M. Lu, J. Li, H. Liu, H. Zhang, Y. Peng, P. Xi, C. H. Yan, *Adv. Mater.* **2020**, *32*, 2001651.
- [2] W. Sun, F. Wang, B. Zhang, M. Zhang, V. Küpers, X. Ji, C. Theile, P. Bieker, K. Xu, C. Wang, M. Winter, *Science* **2021**, *371*, 46.
- [3] J. Zhang, T. Wang, D. Xue, C. Guan, P. Xi, D. Gao, W. Huang, *Energy Storage Mater.* **2020**, *25*, 202.
- [4] C. X. Zhao, J. N. Liu, J. Wang, D. Ren, B. Q. Li, Q. Zhang, *Chem. Soc. Rev.* **2021**, *50*, 7745.
- [5] H. Sun, M. Wang, S. Zhang, S. Liu, X. Shen, T. Qian, X. Niu, J. Xiong, C. Yan, *Adv. Funct. Mater.* **2020**, *31*, 2006533.
- [6] Z. Zhang, X. Liang, J. Li, J. Qian, Y. Liu, S. Yang, Y. Wang, D. Gao, D. Xue, *ACS Appl. Mater. Interfaces* **2020**, *12*, 21661.
- [7] P. Liu, J. Ran, B. Xia, S. Xi, D. Gao, J. Wang, *Nano-Micro Lett.* **2020**, *12*, 68.
- [8] K. Wu, L. Zhang, Y. Yuan, L. Zhong, Z. Chen, X. Chi, H. Lu, Z. Chen, R. Zou, T. Li, C. Jiang, Y. Chen, X. Peng, J. Lu, *Adv. Mater.* **2020**, *32*, 2002292.
- [9] T. Zhou, W. Xu, N. Zhang, Z. Du, C. Zhong, W. Yan, H. Ju, W. Chu, H. Jiang, C. Wu, Y. Xie, *Adv. Mater.* **2019**, *31*, 1807468.
- [10] B. Xia, T. Wang, J. Ran, S. Jiang, X. Gao, D. Gao, *ACS Appl. Mater. Interfaces* **2021**, *13*, 2447.
- [11] H. Liu, D. Zhao, Y. Liu, Y. Tong, X. Wu, G. Shen, *Sci. China Mater.* **2021**, *64*, 581.
- [12] Z. Zhang, H. Sun, J. Li, Z. Shi, M. Fan, H. Bian, T. Wang, D. Gao, *J. Power Sources* **2021**, *491*, 229584.
- [13] X. T. Wang, T. Ouyang, L. Wang, J. H. Zhong, Z. Q. Liu, *Angew. Chem., Int. Ed.* **2020**, *59*, 6492.
- [14] Y. Zhou, S. Sun, C. Wei, Y. Sun, P. Xi, Z. Feng, Z. J. Xu, *Adv. Mater.* **2019**, *31*, 1902509.
- [15] S. L. Zhang, B. Y. Guan, X. F. Lu, S. Xi, Y. Du, X. W. D. Lou, *Adv. Mater.* **2020**, *32*, 2022235.
- [16] D. He, X. Song, W. Li, C. Tang, J. Liu, Z. Ke, C. Jiang, X. Xiao, *Angew. Chem., Int. Ed.* **2020**, *59*, 6929.
- [17] H. Liu, D. Zhao, M. Dai, X. Zhu, F. Qu, A. Umar, X. Wu, *Chem. Eng. J.* **2022**, *428*, 131183.
- [18] D. Zhao, M. Dai, Y. Zhao, H. Liu, Y. Liu, X. Wu, *Nano Energy* **2020**, *72*, 104715.
- [19] D. Zhao, M. Dai, H. Liu, X. Zhu, X. Wu, *Mater. Today Energy* **2021**, *20*, 100637.
- [20] G. Ou, F. Wu, K. Huang, N. Hussain, D. Zu, H. Wei, B. Ge, H. Yao, L. Liu, H. Li, Y. Shi, H. Wu, *ACS Appl. Mater. Interfaces* **2019**, *11*, 3978.
- [21] L. Kumar, P. Kumar, A. Narayan, M. Kar, *Int. Nano Lett.* **2013**, *3*, 8.

- [22] D. M. Morales, M. A. Kazakova, S. Dieckhöfer, A. G. Selyutin, G. V. Golubtsov, W. Schuhmann, J. Masa, *Adv. Funct. Mater.* **2020**, 30, 1905992.
- [23] Y. Yang, L. Liu, H. Zhu, N. Bao, J. Ding, J. Chen, K. Yu, *ACS Appl. Mater. Interfaces* **2020**, 12, 16609.
- [24] X. T. Wang, T. Ouyang, L. Wang, J. H. Zhong, T. Ma, Z. Q. Liu, *Angew. Chem., Int. Ed.* **2019**, 58, 13291.
- [25] S. Sun, Y. Sun, Y. Zhou, S. Xi, X. Ren, B. Huang, H. Liao, L. P. Wang, Y. Du, Z. J. Xu, *Angew. Chem., Int. Ed.* **2019**, 58, 6042.
- [26] R. R. Chen, Y. Sun, S. J. H. Ong, S. Xi, Y. Du, C. Liu, O. Lev, Z. J. Xu, *Adv. Mater.* **2020**, 32, 1907976.
- [27] C. Wei, Z. Feng, G. G. Scherer, J. Barber, Y. Shao-Horn, Z. J. Xu, *Adv. Mater.* **2017**, 29, 1606800.
- [28] J. Gracia, *Phys. Chem. Chem. Phys.* **2017**, 19, 20451.
- [29] J. Yan, Y. Wang, Y. Zhang, S. Xia, J. Yu, B. Ding, *Adv. Mater.* **2020**, 33, 2007525.
- [30] X. Ren, T. Wu, Y. Sun, Y. Li, G. Xian, X. Liu, C. Shen, J. Gracia, H. J. Gao, H. Yang, Z. J. Xu, *Nat. Commun.* **2021**, 12, 2608.
- [31] F. A. Garcés-Pineda, M. Blasco-Ahicart, D. Nieto-Castro, N. López, J. R. Galán-Mascarós, *Nat. Energy* **2019**, 4, 519.
- [32] J. Jang, J. Lee, J. Seon, E. Ju, M. Kim, Y. Il Kim, M. G. Kim, Y. Takemura, A. S. Arbab, K. W. Kang, K. H. Park, S. H. Paek, S. Bae, *Adv. Mater.* **2018**, 30, 1704362.
- [33] Z. He, S. H. Yu, X. Zhou, X. Li, J. Qu, *Adv. Funct. Mater.* **2006**, 16, 1105.
- [34] H. Kato, T. Miyazaki, *Appl. Phys. Lett.* **2004**, 84, 4230.
- [35] F. Caglieris, L. Melone, F. Canepa, G. Lamura, F. Castiglione, M. Ferro, L. Malpezzi, A. Mele, C. Punta, P. Franchi, M. Lucarini, B. Rossi, F. Trotta, *RSC Adv.* **2015**, 5, 76133.
- [36] C. A. Lopez, M. E. Saleta, J. Curiale, R. D. Sanchez, *Mater. Res. Bull.* **2012**, 47, 1158.
- [37] K. L. Pisane, E. C. Despeaux, M. S. Seehra, *J. Magn. Magn. Mater.* **2015**, 384, 148.
- [38] J. Li, Q. Pei, R. Wang, Y. Zhou, Z. Zhang, Q. Cao, D. Wang, W. Mi, Y. Du, *ACS Nano* **2018**, 12, 3351.
- [39] H. Dakhlaoui, M. Nefzi, N. Al-Shameri, A. Suwaidan, H. Elmobkey, S. Almansour, I. Alnaim, *Phys. B* **2020**, 597, 412403.
- [40] J. Qian, T. Wang, Z. Zhang, Y. Liu, J. Li, D. Gao, *Nano Energy* **2020**, 74, 104948.
- [41] Y. Li, L. Zhang, J. Peng, W. Zhang, K. Peng, *J. Power Sources* **2019**, 433, 226704.
- [42] W. T. Hong, M. Risch, K. A. Stoerzinger, A. Grimaud, J. Suntivich, Y. Shao-Horn, *Energy Environ. Sci.* **2015**, 8, 1404.
- [43] S. Chang, H. Zhang, Z. Zhang, *J. Energy Chem.* **2021**, 56, 64.
- [44] L. Gao, S. Chang, H. Zhang, Z. Zhang, *ACS Appl. Mater. Interfaces* **2021**, 13, 22282.
- [45] X. Chen, M. Yu, Z. Yan, W. Guo, G. Fan, Y. Ni, J. Liu, W. Zhang, W. Xie, F. Cheng, J. Chen, *CCS Chem.* **2020**, 2, 675.
- [46] J. Zhang, J. Qian, J. Ran, P. Xi, L. Yang, D. Gao, *ACS Catal.* **2020**, 10, 12376.
- [47] Z. Zhang, G. Yang, J. Wei, H. Bian, J. Gao, J. Li, T. Wang, *J. Cryst. Growth* **2016**, 445, 42.
- [48] S. Verma, P. A. Joy, S. Kurian, *J. Alloys Compd.* **2011**, 509, 8999.
- [49] Z. Wang, Z. Lin, J. Deng, S. Shen, F. Meng, J. Zhang, Q. Zhang, W. Zhong, L. Gu, *Adv. Energy Mater.* **2020**, 11, 2003023.
- [50] Q. Song, J. Li, S. Wang, J. Liu, X. Liu, L. Pang, H. Li, H. Liu, *Small* **2019**, 15, 1903395.